 doi:10.20944/preprints202106.0366.v1

Article

Deposits' Morphology of the 2018 Hokkaido Iburi-Tobu Earthquake Mass Movements from LiDAR & Aerial Photographs

Gomez, Christopher[1], and Hotta Norifumi[2]

[1] Kobe University, Laboratory of Sediment Hazards and Disaster Risk; christophergomez@bear.kobe-u.ac.jp
[2] Graduate School of Agricultural and Life Sciences, Department of Forest Science, The University of Tokyo; hotta.norifumi@fr.a.u-tokyo.ac.jp
* Correspondence: christophergomez@bear.kobe-u.ac.jp

Abstract: On September 6th, at 03:08AM local time, a 33 km deep earthquake underneath the Iburi mountains triggered more than 7,000 co-seismic landslides within 25 km of the epicenter. Most of the landslides occurred in complex terrain, and became coalescent. But a total of 59 landslides, occurred as discrete events and stopped on semi-horizontal valley floor. Using this sample, the authors aimed to define planar and vertical parameters for hazards purpose and for the characterization of the mass-movement geometry triggered by the Hokkaido Iburi-Tobu Earthquake.The aim of the present contribution was to contribute to the existing databases of empirical relationships based on planform and vertical dataset, and to define the scalars of those relations that characterize the mass-movements of the Iburi-Hokkaido earthquake, with the overarching goal of generating predictors for hazard-mapping. To reach these objectives, the methodology relies on LiDAR data flown in the aftermath of the earthquake as well as aerial photographs. Using Geographical Information System (GIS) tools planform and vertical parameters were extracted to calculate the power-law relations between areas and volume, between the Fahrböschung and the volume of the deposits, as well as other geometric relationships. Results have shown that the relation $S = k[V_d]^{2/3}$ where S is the surface area of a deposit and V_d the volume, and k a scalar that is function of S: k=2.1842 ln(S)-10.167 with a R^2 of 0.52, and this relation is improved for the open-slope mass-movements but not the valley-confined ones, that present more variability. The Fahrböschung for events that started as valley-confined mass-movements was Fc = -0.043ln(D) + 0.7082 with a R^2 of 0.5, while for open-slope mass-movements, the Fo = -0.046ln(D) + 0.7088 with a R^2 of 0.52. These results contribute to the growing co-seismic landslide database and they can also be the base to understand the role of the counter-slopes and complex topography on the spread and distance travelled by the mass-movement deposits.

Keywords: Landslide; LiDAR; Deposit morphology

1. Introduction

The world population is increasingly urban, leaving vasts areas of 'green deserts' sometimes located at the door-step of human settlements. Therefore, events triggered in those peripheries call for control and management to limit hazards and disaster risk. In those areas of lesser accessibility, remote sensing is consequently playing an essential role in data collection and analysis, especially in countries where population is ageing and manpower is coming at a premium. It is therefore within this framework that the present contribution investigated the morphological parameters of individual co-seismic mass-movements, emphasizing the need to be able to work from remote-sensing data solely.

1.1. The 2018 Hokkaido Iburi-Tobu (HIT) Earthquake and the coseismic mass-movements

On September 5th, 2018 at 18:07 UTC (September 6th, at 03:08AM local time), a magnitude 6.6 earthquake shook the Iburi-Tobu region - South of Hokkaido, Japan (Fig. 1).

Preprints (www.preprints.org) | NOT PEER-REVIEWED | Posted: 14 June 2021 doi:10.20944/preprints202106.0366.v1

The shallow earthquake (33 km depth) was the result of a reverse-slop fault movement, which resulted in approximately 7059 landslides (Fig. 1) within an area of 466 km² (Zhao et al., 2020). Furthermore, remote sensing –based spatial analysis has shown that the density of mass-movements was up to 95/km² (Bo et al., 2020), and that this density was related to the surface area by the relationship:

$$\mathbf{y = 110 * e^{[-\log(x) - \frac{3.26)^2}{0.2378}]}} \quad (1)$$

where y is the number of landslide for a given x surface area (Zhao et al., 2020).

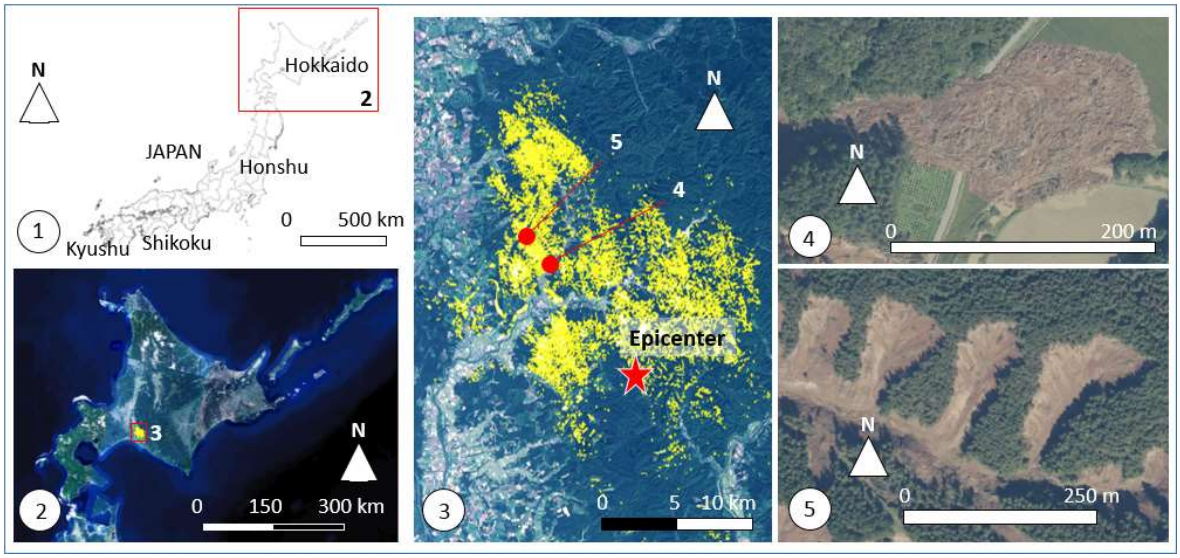

Figure 1. The Hokkaido Iburi-Tobu Earthquake of 2018. (1) Map of Japan indicating the position of Hokkaido island and prefecture; (2) Location of the Research location in the Southern Part of Hokkaido; (3) Location of the epicenter symbolized by a red start and the digitized landslides in yellow. The locations of photographs 4 and 5 are also provided. (4) Landslide mixing sediments and wood debris that stopped on a pseudo-horizontal valley floor – the object of the study. (5) Landslides with mixed deposits on slopes and constrained within narrow valleys – not used in the present study.

The large number and high-density of mass-movements can be first explained by the seismic and geologic realm of the event. The earthquake is believed to be the result of a local crustal weakness, which reacted to the regional strain accumulation (Ohzono et al., 2019). The sudden energy release is supposed to have originated from a major slip along the faulting plane (Kobayashi et al., 2019; Kubo et al., 2020). This subterranean slip then translated at the surface into strong motion, notably under the amplification of the near-subsurface structure (Takai et al., 2019). As the near-subsurface is made of +/- 9,000 years old air-fall lapilli-sized pumice soil layers (about 1.5 m thick), which draped the Neogene sediment formations (Yamagishi and Yamazaki, 2018), it creates a stratigraphic discontinuity, which have been pressed forward as an explanatory factor of the high-density of mass-movements.

Besides the geological factors, heavy antecedent rainfalls that occurred before the earthquake contributed to destabilizing the slopes. The HIT earthquake occurred one day after Typhoon Jebi (Typhoon 21 of the year 2018) had swept over the area, pouring a cumulated 100 mm rainfall over 3 days (Yamagishi and Yamazaki, 2018). One can then logically suppose that the slope shear strength was weakened before the HIT earthquake occurred.

 doi:10.20944/preprints202106.0366.v1

Because of the combination of both the typhoon and the earthquake, scientists have proposed that one of the two parameters were at the origin of the high number and density of landslides. However, due to the local variation and temporal variation of soil mechanical properties, physically-based deterministic models remain elusive to scientists who have to work statistically from databases (Chang et al., 2020). Consequently, the present work aims:

(1) to contritbute to existing databases of the morphology of mass-movement deposits and how they relate to the watershed morphometry they flow in;

(2) to provide an insight into the 3D geometrical relationships of the deposits in the area impacted by the HIT-earthquake, as existing work has been so far focused on the spatial distribution of the events and the 2D characterization of the mass-movement deposits.

This research finds further motivation in the fact that most landslides are either rainfall-triggered or seismically-triggered, but more rarely the result of the two factors combined, for which further research is needed (Calista et al., 2019; Pu et al., 2021), eve in areas of relatively low seismic activity (Bo et al., 2020).

1.2. The mapping of mass-movements from aerial remote-sensing platforms

Mass-movements can be either very-slow and deep-seated (Morelli et al., 2018) or more shallow events, such as rotational, planar slides, rock falls, debris flows (Agliardi et al., 2001), displaying surface deformation at a variety of scales (from the all mountain down to a few meters across). For the study of mass-movements, there exists a broad range of remote-sensing platforms. They range from satellite-platforms (Bovenga et al., 2006; Thomas et al., 2016) down to airborne, UAV and Ground-based laser techniques and photogrammetry (Gomez et al., 2021). Although remote-sensing is now sufficiently developed to generate datasets without contact-data, aerial photo-analysis for instance has long been considered as a complement to field surveys (Strozzi and Ambrosi, 2007). And even methods that have risen in recent years, such as structure-from-motion from aerial photographs (Gomez et al., 2015) and UAV (Clapuyt et al., 2016), still needs ground control data (Mateos et al., 2017; Peternal et al., 2017; Eker et al., 2018). Remote sensing has therefore considerably helped in the field of detection and mapping of landslides, and in areas where no precursory signs are detectable, remote-sensing can be further used to understand the mechanisms of triggering, movement and deposition. The geometric characteristics of the landslides can then be used to develop empirical models for hazard and disaster risk management.

1.3. Empirical relationships for mass-movements

Using remote-sensing platforms and field surveys, scientists have put the emphasis on the generation of descriptive and explanatory metrics describing the morphology of the triggering zones and deposits. Such metrics are essential to compare mass-movements between events and between one location and another.

The mass movements of the HIT earthquake are mostly shallow rapid-onset events, involving a mixture of soils and wood debris. These characteristics relates the events to the classes of debris-flows and debris-avalanches, which have been defined as: “rapid to extremely rapid shallow flow of partially or fully saturated debris on a steep slope, without confinement in an established channel” (Hungr, 2005 p.15).

For the characterization of mass movement deposits, and especially debris0flows, researchers have developed a set of morphological metrics. Scheidl and Rickenmann (2010) have expressed the relation between the deposit basal area S and the volume V using the following relation:

$$\mathbf{S} = \boldsymbol{K'_B V^{\beta}} \quad (2)$$

, which is the same expression that Crosta et al. (2003) used and for which they determined $\boldsymbol{V^{\beta}}$ to be 2/3, and $\boldsymbol{K'_B}$ to be equal to 6.2. This equation comes from two power-law relations between the size of the deposit and the volume on one hand, and between

 doi:10.20944/preprints202106.0366.v1

the flow cross-section and the volume of the deposit on the other hand (Iverson et al., 1998).

On top of the planform relation of the deposit, other indicators relate the deposit to the geometry of the catchment where the mass-movement started. The most concised approach links the vertical and horizontal translation to the volume of the mass transported, providing an empirical assessment of potential hazards. This relation has been famously expressed as the Fahrböschung, which is expressed as the angle between the highest starting point of a landslides, and the furthest point the translated mass reaches. Other empirical relations have similarly linked the travel angle starting from the centre of gravity of the mass to be translated (before sliding) to the centre of mass of the deposit (Corominas, 1996). For volume of 1E+02 m^3 to 1E+06 m^3 from Swiss debris flow, the travel angle – tan β – varied between less than 0.1 to 0.8 with a trend showing a decrease in the travel angle with the increase of the volume of the debris flows (Corominas, 1996). However, the variability in the dataset hardly makes it a prediction tool on its own, as tan β varies from 0.2 to >0.6 for 1+E3 m^3 debris flow and from < 0.1 to 0.5 for debris flows around 1E+5 m^3 volume. Rock avalanches and landslides also show similar patterns but for a different relationship between the two variables (Rickenmann, 2005). These relations were formulated by Corominas (1996) as:

$$\log\left(\frac{H}{L}\right) = -1.05 \log V - 0.012 \quad (3)$$

where H is the vertical difference and L the horizontal distance and V the volume, and in a different form, Rickenmann (1999) found a relation with $R^2 = 0.75$ for 160 debris flows expressed as:

$$L = 1.9V^{0.16}H^{0.83} \quad (4)$$

Therefore, from the Northern American mountains, to the European New-Zealand and Japanese Alps, an abundance of debris-flows has been instrumental in developing these empirical relationships.

Building on this legacy of shape-factors construction, the present research contributes a set of calculations for mass movements triggered by a combination of rainfall and seismic activity. The objective is therefore to calculate geometric relations for the landslides triggered by the 2018 HIT Earthquake, using aerial photographs and LiDAR data, to improve hazards and disaster risk management.

2. Methodology

The present work is interested in generating comparable and "reusable" data, and therefore a selection of landslide with "simple" landform geometries was chosen: (1) landslides that can be clearly identified as being one unit separated from another, and (2) landslides that were not adversely affected by complex topography in the deposition area (deposition on flat valley floors).

2.1. Data acquisition: Information Retrieval from Lidar and Aerial Photographs using GIS

The data used in the present research have been orthophotographs (10 cm resolution) created from aerial photographs taken in the immediate aftermath of the event and a LiDAR-based DEM. The DEM is a 52,000 pixels by 45,000 pixels gridded data of pixel size 0.5 m x 0.5 m projected in JGD2011 making a set of tiles of 10.8 km x 21.5 km. The aerial photographs resolution is 0.1 m x 0.1 m. Both datasets were produced by the Japanese Government Ministry of Land Infrastructure and Transport.

Using the open-source environment QGIS3.14, the orthorectified tiles of aerial photographs were combined into one single file. The same operation was applied to the DEM tiles as well. Using shapefiles to delineate the planform of the mass-movement deposits and make calculations over the raster images, a total of 59 landslides was mapped. The choice of the 59 landslides was based on two conditions: (1) each mass-movement deposit

Preprints (www.preprints.org) | NOT PEER-REVIEWED | Posted: 14 June 2021 doi:10.20944/preprints202106.0366.v1

was clearly separated from other deposits without mixing, and (2) the deposits had to stop over a pseudo-horizontal area such as a valley-floor, a paddy-field, and so without having to climb on a counterslope. The majority of the mass-movements occurred in the mountains and had coalescent deposits that were not suited for the present analysis, and thus were discarded. For each mass-movements, the following planform data was acquired: the total travel distance, the width of the landslide deposits, and the length of the landslide deposits; as well as the following vertical data: the elevation difference between the crown of the mass-movement and the toe of the deposit, the height difference between the upstream elevation and the apex elevation, as well as the mean elevation of the deposit (Fig 2).

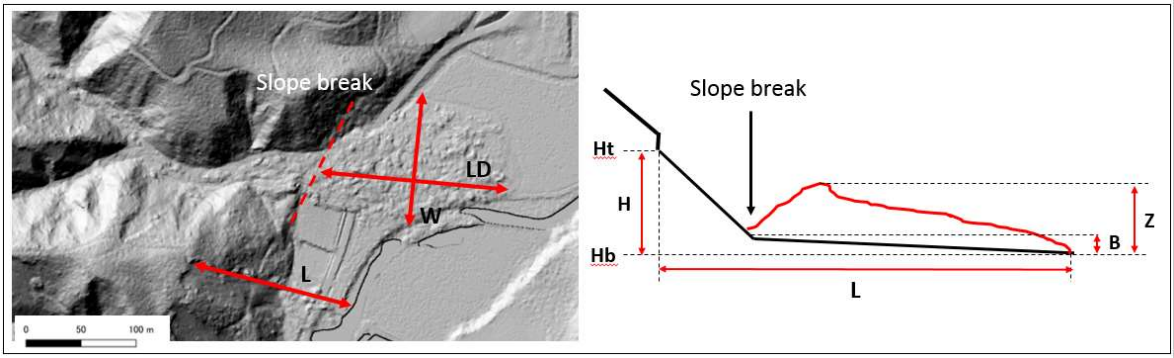

Figure 2. The basic linear parameters used to calculate the geometric data as well as the empirical factors (L: maximum horizontal distance travelled by the mass-movement; W: maximum width of the deposit; LD: maximum horizontal length of the deposit pass the slope break; Ht: Maximum elevation at the scarp the landslide started from; Hb: Minimum elevation at the toe of the deposit; H: Difference of Hb subtracted from Ht; Z: the maximum height of the deposit, used to calculate the slope of the deposit's surface; B: the elevation of the underlying topography at the slope break and at the toe of the deposit).

The parameters were then combined geometrically to estimate the volume of deposits D, with Z and Bs respectively representing the vertical and horizontal components of the volume downstream of the slope break (eq. 5) :

$$\mathbf{D} = \sum_{\mathbf{i=1}}^{\mathbf{n}} \mathbf{Z_i} - \sum_{\mathbf{i=1}}^{\mathbf{n}} \mathbf{Bs_i} \quad (5)$$

To calculate the fahrböschung (which is given here as simply the ratio of the height to the distance travel), we used the following relation:

$$\mathbf{F} = \frac{\boldsymbol{Ht - Hb}}{\boldsymbol{L}} \quad (6)$$

The fahrböschung is often expressed in degrees, but in the text we refer to H/L as the fahrböschung (the reader can transform it into an angle when suited).

2.2. Empirical analysis

After creating the geometric indicators, the next methodological-step is an empirical analysis of the relations between the different morphological factors. This analysis relies on geometric equations and the power-law by Crosta et al., (2003) as:

$$\mathbf{S} = \mathbf{k}\boldsymbol{V_d}^{\mathbf{2/3}} \quad (7)$$

Where S is the surface area of the deposit, and V_d is the volume of the deposit, with k being a scalar depending on the type of flow and the event recorded. Using the empirical data generated by remote sensing, the value(s) of k has been calculated and compared to

 doi:10.20944/preprints202106.0366.v1

other landslide parameters, to see whether the parameter is stable regardless of the slide considered or, on the contrary whether the relation changes.

Another scalar that was investigated is the one developed for rain-triggered debris-flows, and it seems to apply well to the present problem as the deposits have been described as "debris-flow –like" (Zhao et al., 2020) and because the relation relates the fanning surface A and the volume of the debris-flow as (Takahashi, 2014) so that it can be extracted from the deposits morphology:

$$\boldsymbol{T = \frac{V_d}{S^{3/2}\tan(\gamma_d - \theta_d)}} \quad (8)$$

Where T=5/12 for debris-flows, $\boldsymbol{\gamma d}$ is the slope surface downstream-ward, and $\boldsymbol{\theta d}$ is the basal slope underneath the deposit (Takahashi, 2014, eq. 5.61 p. 274). This equation has the advantage of being more grounded into the realm of landslides as it takes into account the slope angles where the material deposited as well as the slope of the surface of the deposit that is a proxy of the internal friction angle and the velocity during deposition.

Those empirical relations are mathematical and grounded in geometric relations instead of physical ones, so that they are adapted to hazards and disaster risk management to make predictions of the hazard zones, but they do not aim to explain the physics of the landslides.

3. Results

In this section, the authors present the geometrical relations between the morphological parameters and between the different shape indicators and factors, before ending with data on the distribution of the tree stems deposited over the sediments.

3.1. The geometry of the deposits on pseudo-horizontal surfaces

The investigated mass-movements are shallow, with slip surfaces located within 2 m depth from the surface for valley-confined mass-movements and within 3.5 m depth for open-slope mass-movements, based on the steps generated at the scarps where the landslide started from. The average deposit surface area is 8271 m^2 with the smallest event being 172 m^2 and the largest one 25510 m^2 . The average length of the deposit was 133 m and the minimum length 24 m and the maximum length 283 m. One of the important factor is the ability of the material to spread while depositing. The relation between the width (W) and the length of the deposit (LD) could be expressed with the following power law (Fig. 3) as:

$$\boldsymbol{LD = 2.2492W^{1.0296}} \quad (9)$$

Interestingly, the type of landslides on open-slope and in confined valleys do not statistically influence the relation between the length and the width of the deposit as the empirical values agree with the model following a $R^2 = 0.8985$.

Preprints (www.preprints.org) | NOT PEER-REVIEWED | Posted: 14 June 2021 doi:10.20944/preprints202106.0366.v1

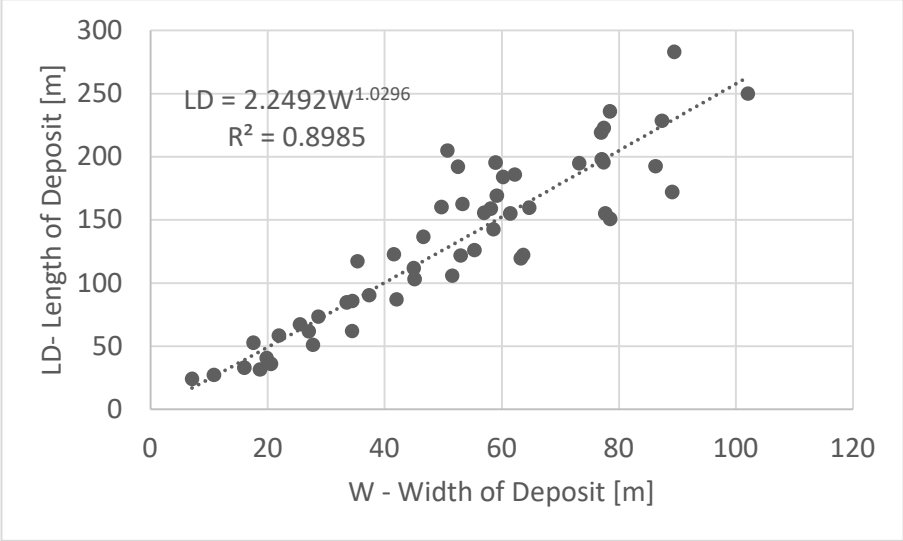

Figure 3. Relation between the width of the deposits and the length of the deposits for all the samples that stopped on pseudo-horizontal valley floor.

3.2. Surface - volume relations of the deposits

For the investigated landslides, the k value (eq. 7) is varying with the size of the area of the deposit, so that the power-relationship of equation 7 accepts an array of k-values. The k-values relate to the surface area of the deposit following a logarithmic relation (Fig. 4):

$$\boldsymbol{k = 2.1842\, ln(S) - 10.167} \quad (10)$$

Although the graphic representation seems to indicate that there are potentially two different logarithmic relations (Fig. 4), the two are not a spatial relationship to the epicenter nor the relation to a valley or a preferred orientation. The division between valley-confined and open-slope landslides also show differently, with two k – the "o" and "c" subscript refer to open-slope and valley-confined respectively - that are (Fig. 5):

$$\boldsymbol{k_o = 2.2993\, ln(S) - 10.901} \quad (11)$$

$$\boldsymbol{k_c = 2.1308\, ln(S) - 10.124} \quad (12)$$

And while ko displays a R^2 of 0.62 +/- 10%, the kc is only at 0.35 +/- 10%, showing in the second case a greater variability in the dataset. The graphic representation gives clues to this variability, as a cluster of landslides of 8,000 to 12,000 m2 are systematically below the predictive curves relating kc to S.

Preprints (www.preprints.org) | NOT PEER-REVIEWED | Posted: 14 June 2021 doi:10.20944/preprints202106.0366.v1

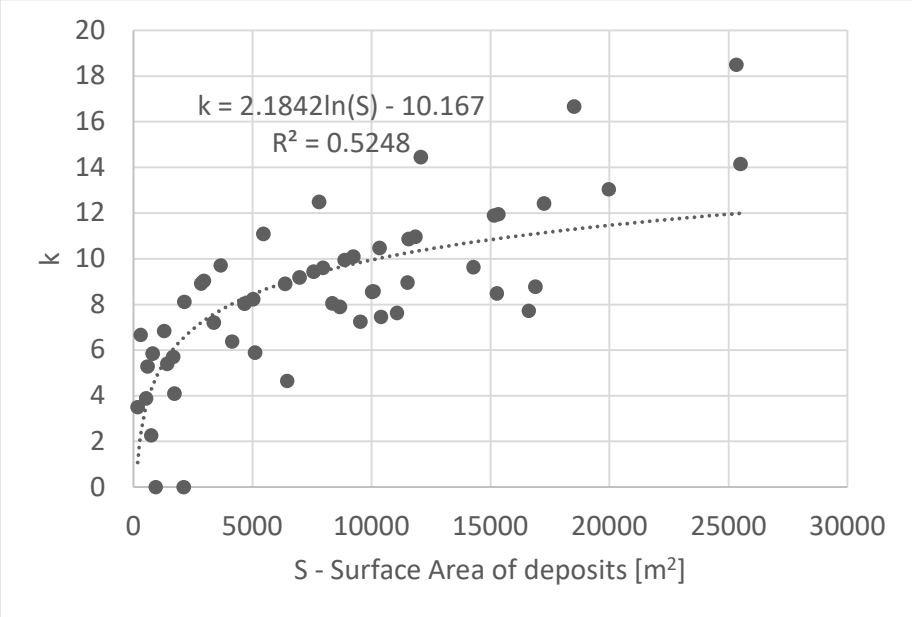

Figure 4. Relation between the power-relation scalar k (eq. 7) and the surface of the deposits.

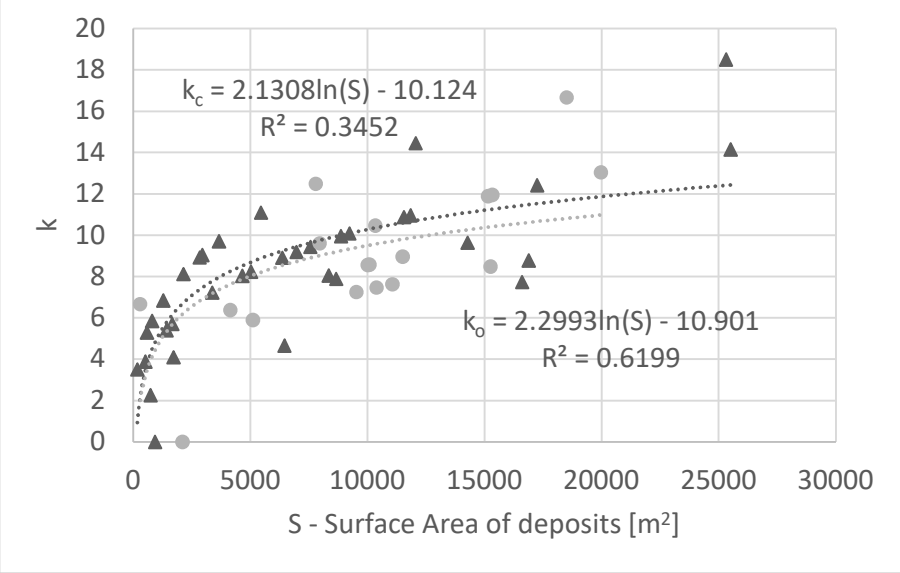

Figure 5. Relation between the power-relation scalar k (eq. 7) and the surface of the deposits, separating the open-slope landslides (dark grey triangles) and the valley-confined landslides (light grey circles). The subscripts "o" and "c" refer to the open-slope- and the confined- landslides.

The second scalar that was investigated, and which has been developed for debris-flow is the T-scalar, which is the empirical factor calculated for equation 8. As the base slope underneath the mass-movement deposits (θ_d) has been one of the variable kept close to a constant by "choosing" landslides that had stopped on sub-horizontal surfaces, the variability in the T scalar is therefore a function of the slope surface of the deposits, and the Area-Volume correlation. Except for three outliers, the data are bounded by an upper limit at T = -0.0001 S+ 3.75, while the two dataset relates to one another with T = -0.0001S + 2.9497, but very poorly (R^2 = 0.0108).

Preprints (www.preprints.org) | NOT PEER-REVIEWED | Posted: 14 June 2021 doi:10.20944/preprints202106.0366.v1

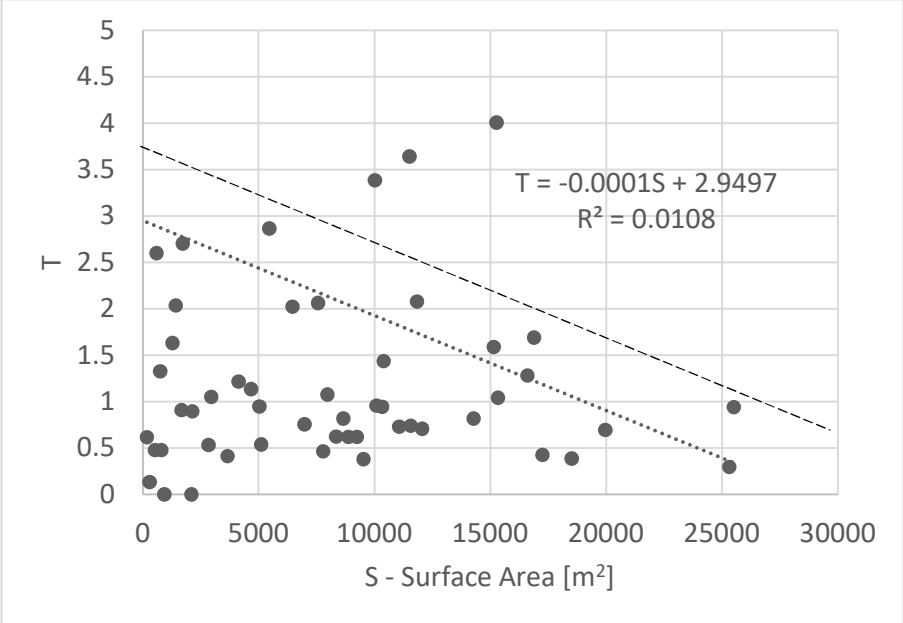

Figure 6. The relation between the Surface area and the T scalar relating the volume to the area and the slope gradient of the deposit, allowing for ~5% outliers.

3.3. The fahrböschung for "open-slopes" and "Valley-confined" flows

The fahrböschung is comprised between 0.15 and 0.55 +/- ~5% (allowing 3 outliers), and it decreases as the volume of the deposit increases. The smallest landslides < 4,000 m^3 have all a fahrböschung > 0.3, while the landslides with a volume > 59,000 m^3 are all below 0.2. Those to end-member groups link through a constantly decreasing F as V increases, following a relationship (Fig. 7a) as follows:

$$F = 0.3521^{-9*10^{-06}D} \quad (13)$$

Separating the two types of landslides (valley-confined and open-slope), there is once again no clear distinction between the two types of movements and they seem to have relatively similar mobility (Fig. 7b), as represented by the two relation equations (Eq. 14 and 15):

$$F_c = -0.043\ln(D) + 0.7082 \quad (14)$$

$$F_o = -0.046\ln(D) + 0.7088 \quad (15)$$

As the fahrböschung is a proxy of the mobility of the landslides, one authors hypothesized that it should have a linear effect on how the material spreads. Comparing the ratio of width per length of deposit (W/LD), this ratio SF was computed against F (Fig. 9). There is no strong linear correlation between the two dataset, because of a seemingly not varying fahrböschung set of data F < 0.1, but an envelope with a positive trends appears, with the mass-movements with the lowest-mobility being the one that tends to spread the most (Fig. 8).

Preprints (www.preprints.org) | NOT PEER-REVIEWED | Posted: 14 June 2021 doi:10.20944/preprints202106.0366.v1

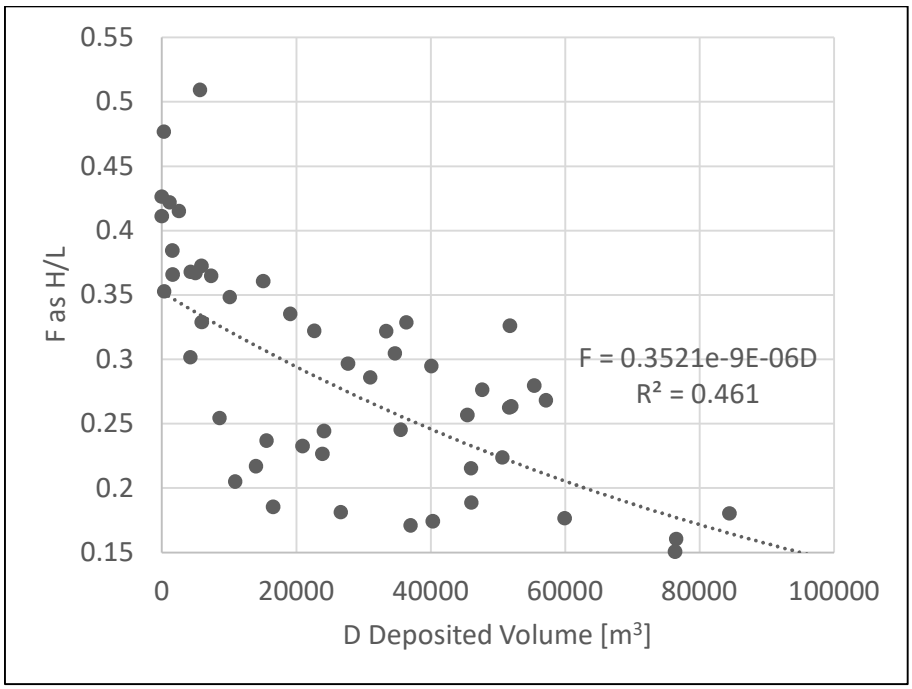

(a)

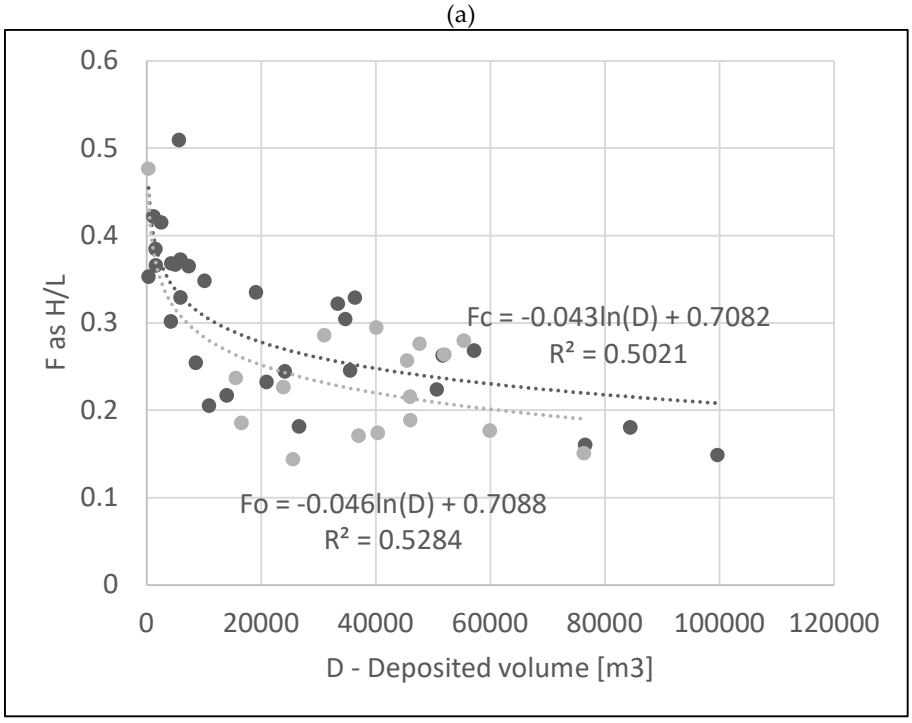

(b)

Figure 7. (a) The fahrböschung F calculated against the volume of the deposits for the selected landslides. (b) Relation between the deposited volumes and the fahrböschung (F) separating the deposits from valley-confined mass-movements (Fc) and the deposits resulting from open-slope mass-movements (Fo). Both display comparatively similar fahrböschung relations.

Preprints (www.preprints.org) | NOT PEER-REVIEWED | Posted: 14 June 2021 doi:10.20944/preprints202106.0366.v1

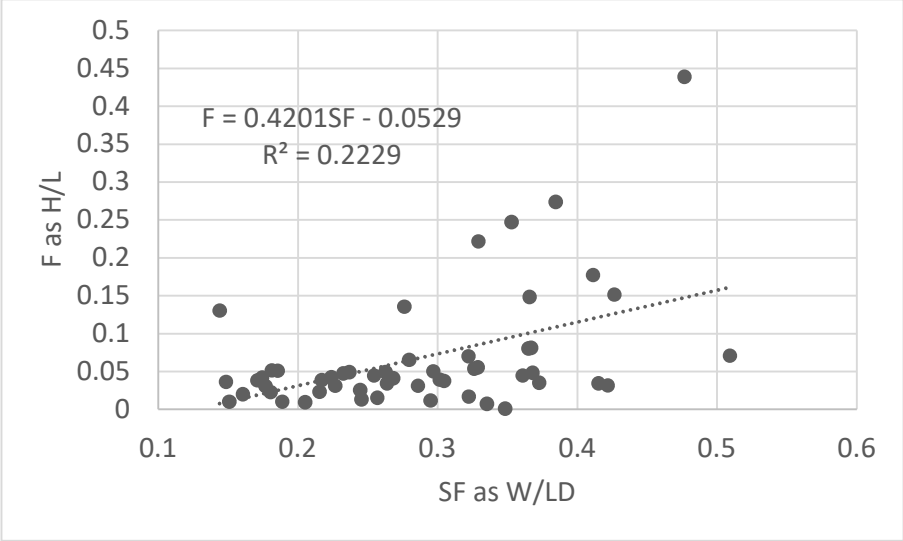

Figure 8. The Fahrböschung F as a function of SF, being the ratio of the width to the length of the deposit, showing its ability to spread laterally.

4. Discussion

4.1. Result summary

The mass-movements measured from LiDAR and aerial photographs remote sensing are relatively homogeneous in term of deposits geometry following the relation LD = $2.2492W^{1.0296}$ with a $R^2 = 0.8985$. If one considers this geometric relation as being the result of mass-movements ending on a sub-horizontal surface, it is then possible to compare these results with the deposits of mass-movements that have stopped on counter-slopes to investigate the role of the latter for instance. The k-parameter follows a k=2.1842 ln(S)-10.167 relation with the surface area of the deposit, with variations depending on whether the deposit was created by an open-slope or a valley-controlled landslide (equations 11 and 12). The T parameter was more spread and could not lead to any significant relation, if not for the construction of an empirical ceiling-function. The fahrböschung followed a typical pattern, with the larger deposit-volumes displaying a F inferior to the ones of smaller landslides: the deposits generated from valley-confined movements yielded a fahrböschung of Fc= -0.043ln(D)+0.7082 with an $R^2 = 0.5021$, while the open-slopes' movements displayed a Fo = -0.046ln(D)+0.7088 with $R^2 = 0.5284$.

4.2. The Hokkaido Iburi-Tobu Earthquake landslides were extremely mobile

The fahrböschung, whether it is expressed as an angle or as a ratio height to length is a useful comparator of the mobility of landslides that has been shown to decrease with the mass and volume landslides At the Naga landslide for instance, Lagmay et al (2020) calculated a fahrböschung (as H/L) of 0.17 (or 9 degrees), while Catane et al (2019) calculated 0.16 (or 9 degrees), for estimated volumes of 11 and 27 million cubic meters respectively. At the Guinsaugon landslide (February 2006, Leyte Island, Philippines), Evans et al. (2007) calculated 0.21, and Lagmay et al. (2008) 0.17, with in both cases, volumes of 15 million cubic meters On 23 September 1991, the rock avalanche of Zhaotong (China)travelled 3650 m horizontally for a vertical drop of 960 m, resulting in a fahrböschung of 14.7 degrees or 0.263 expressed as H/L (Xing et al., 2016). If we use the relation obtained in the present study between H/L and V (as H/L = 0.046ln(V)+0.7088), the present-formula is much lower (it gives for instance 0.028 for the 27 million cubic meter Naga landslide, instead of the measured 0.16).

This suggests that the Iburi-Tobu Hokkaido earthquake landslides were extremely mobile compared to other values found in the literature. Direct comparisons of different landslides is however arduous, because of the variety of flowing processes, materials and

grain-size. For granular flow for instance, Coombs et al (2020) have shown that the fahrböschung decreased by 14% from 25 to 21.4 degrees when the mean grain sizes in the experiments is changed from 3 to 25 mm. Besides the original grain-size effects, the self-comminution of the grains impact stability and shear strength (Gomez et al., 2020) and so is the presence of volcanic material in soils, as it has been shown in other locations in Japan (Yamanouchi and Murata, 1973). This work found that the dry density could be as low as 13 to kN/m^3, values that are comparable to the 10 to 15 kN/m^3 found in Tenerife (Gonzalez de Vallejo et al., 1981) or 11 to 14 kN/m^3 for the Cangahua volcanic soil formation in South America (O'rourke and Crespo, 1988).

Because of the variability of parameters at play, the authors reduced the sum of these issues to the Mohr-Coulomb effective stress theory to discuss the high-mobility of the Hokkaido Iburi-Tobu coseismic landslides from a practical perspective. In its simplest form, the Mohr-Coulomb failure criterion can be expressed as:

$$\boldsymbol{\tau_f = C' + \left(\sigma_f - u_w\right)_f tan\, \varphi'} \quad (16)$$

Where the term on the left is the maximum stress a soil allows before failing, the first term on the right side of the equation is the cohesion, the second term is the effective stress multiplied by the tangent of the angle of friction. This equation can be used to describe the state of a material on a slope, but a non-linear envelops is needed to take into account the seismic loading (Zhang and Chen, 1987) and expressed with a linear coefficient (Zhao et al., 2017) as follow:

$$\boldsymbol{\tau = C_0 * \left(1 + \frac{\sigma_n}{\sigma_1}\right)^{1/m}} \quad (17)$$

where, is the shear stress σ_n is the normal stress, $\sigma_1$is the intercept of the envelope shear stress with the normal stress axis (Zhao et al., 2017), $C_0$is the cohesion and 1/m is the non-linear parameter. Because the present contribution is a remote sensing contribution, and not a geotechnical analysis, the goal is not to solve these equations, but to compare the two in order to reflect to the unusually long runout, and low H/L even when the landslide volumes were small.

From equation 17, when m is more or equal to 1, the Mohr-Coulomb envelope is therefore rising at a lower rate than the linear Mohr-Coulomb envelope, so that for a similar slope the normal stress that the slope can sustain before failing is lower under seismic activity.

By this process, the authors would argue that there may be a reduction of the "local effects" explaining the relative homogeneity in the shapes of the landslides (cf. equation 9 with a R2 = 0.89). This effect needs further evidence and investigation, but potential research direction certainly includes the role of the shaking during the movement, limiting deposition due to local effects, and also the homogeneous start of the mass movements. As rainfall will poor more on one catchment than another, heterogeneity in the mass movements may arise. Finally, the factor of safety of each slope may become irrelevant when considering the threshold, as intense surface acceleration may produce energy throwing all the slopes way above their factor of safety threshold. This would then homogenize the mass-movements, limiting local factors.

Remote sensing effectiveness could thus be increased in combination with high-resolution rainfall data and geo-mechanical data, and this is the last discussion point I would like to mention. I believe that in the same way geologists and topographers have made maps of the surface of the Earth and the formations, we need to develop high-resolution maps of shear strength of soils if we want to improve significantly present models.

Conclusion

High-Resolution Topographic data combined with remotely-sensed imagery has been shown to be an effective tool in generating sets of descriptive parameters of landslide

deposits. The correlation between the width and length of the deposit have shown a good correlation, suggesting that the conditions of lateral spreading during deposition were all relatively similar. This is often not the case with rain-triggered landslides, because the internal friction and cohesion can show wide variability, but in the present case, the seismic excitation at the scale we are working is rather similar, and so is the material. So that at the micro-scale the "excitation of particles" tends to converge, and during the deposition process, this convergence may have contributed to create planform relations of length to width that are very similar. However, the T parameter developed for debris-flow, has shown weak correlation with the parameters of shape and volume. We interpreted this weak correlation as being eventually the effect of continuous excitation by the earthquake. It is not a balance of potential energy at the start being dissipated with movement, we need to take into account the input of seismic energy over time while the landslide is travelling. This dataset can be used to evaluate the areas where deposits are likely to develop based on other pre-event topographic data, and by then quantify hazards and disaster-risk around earthquake-prone hills and mountains. This work also emphasizes the need to develop further database of landslide parameters, so that those can be compared in order to define specificities of one location or another.

The present research has shown the exceptional mobility of the landslides, and one research direction that spans beyond the realm of remote sensing, is the field investigation of the potential influence of volcanic fallout, as it is often the case in Japan. I would further argue that increasingly adding "tele-connections" between landforms and soil formation is certainly a direction that is necessary, in the same way they have been shown to play a potential role in linking tsunamis and mountain debris flows through atmospheric teleconnections (Gomez and Soltanzadeh, 2012).

Author Contributions: "Conceptualization, Christopher Gomez. and Norifumi Hotta; methodology, validation, Christopher Gomez; project administration, Norifumi Hotta.; funding acquisition, Norifumi Hotta. All authors have read and agreed to the published version of the manuscript.

Funding: The present contribution is funded by the Japanese national scientific grant Kakenhi A 18H03957.

Acknowledgments: The authors are also in dept to three anonymous reviewers and the editorial team for careful consideration of the present contribution. The authors would like to also thanks the reviewers who took the time to provide suggestions with the write up on top of the scientific content.

Notations:

C': effective cohesion

D: Deposit volume calculated from the LiDAR data assuming a flat underlying layer and no erosion [m3]

F: fahrböschung [no unit]

k: the factor relating volume to area [1/m]

LD: Length of the deposit [m]

S: Surface of the deposit calculated from the LiDAR and aerial photographs [m2]

SF: Ratio of the width to the Length of the deposit [no unit]

T: One of the scalar used in Takahashi's equations relating debris flow volume to area [1/m]

W: Maximum width of the deposit measured near or at the centre [m]

τ_f: Shear stress along the failure plane

σ_f: total normal stress along the plane of failure

φ': effective angle of internal friction

u_w: the stress due to the water in the grain interspace.

Conflicts of Interest: The authors declare no conflict of interest. The funders had no role in the design of the study; in the collection, analyses, or interpretation of data; in the writing of the manuscript, or in the decision to publish the results.

References

1. Agliardi F, Crosta GB, Zanchi A (2001) Strutural constraints on deep-seated slope deformation kinematics. Engineering Geology 59, 83-102.
2. Bo Z, Yunsheng, W, Qianqian F, Fengshuang G, Zhao X, Ji F, Jiangwei L, Ming W (2020) Preliminary analysis of some characteristics of coseismic landslides induced by the Hokkaido Iburi-Tobu earthquake (September 5, 2018), Japan. Catena 189, 104502:1-11.
3. Bovenga F, Nutricato R, Refice A, Wasowski J (2006) Application of multi-temporal differential interferometry to slope instability detection in urban/peri-urban areas. Engineering Geology 88, 219-240.
4. Calista M, Miccadei E, Piacentini T, Sciarra N (2019) Morphostructural, Meteorological and Seismic Factors Controlling Landlsides in Weak Rocks: The Case Studies of Castelnuovo and Ponzano (North East Abruzzo, Central Italy). Geosciences 9, 122, 1-31.
5. Catane, S., Veracruz, N., Flora, J., Go, C., Enrera, R., and Santos, E. (2019). Mechanism of a low-angle translational block slide: evidence from the September 2018 Naga landslide, Philippines. Landslides 16, 1709–1719. doi: 10.1007/s10346-019-01212-9
6. Chang, M., Zhou, Y., Zhou, C., Hales, T.C. 2020. Coseismic landslides induced by the 2018 Mw 6.6 Iburi, Japan, Earthquake: spatial distribution, key factors weight and susceptibility regionalization. Landslides https://doi.org/10.1007/s10346-020-01522-3
7. Clapuyt F, Vanacher V, Oost KV (2016) Reproducibility of UAV-based earth topography reconstructions based on Structure-from-Motion algorithms. Geomoprhology 260, 4-15.
8. Coombs SP, Apostolov A, Take WA, Benoit J (2020) Mobility of dry granular flows of varying collisional activity quantified by smart rock sensros. Canadian Geotechnical Journal 57-10, https://doi.org/10.1139/cgj-2018-0278.
9. Corominas J (1996) The angle of reach as a mobility index for small and large landslides. Canadian Geotechnical Journal 33, 260-271.
10. Crosta GB, Cucchiaro S, Frattini P (2003) Validation of semi-empirical relationships for the definition of debris-flow behavior in granular materials: in Debris-Flow Hazards Mitigation, Rickenmann and Chen (Eds.) Millpress, Rotterdam, p. 821-831.
11. Eker R, Aydin A, Hubl J (2018) Unmanned aerial vehicle (UAV)-based monitoring of a landslide: Gallenzerkogel landslide (Ybbs-Lower Austria) case study. Environmental Monitoring and Assessment 190:28, 1-14.
12. Gomez C, Allouis T, Lissak C, Hotta N, Shinohara Y, Hadmoko DS, Vilimek V, Wassmer P, Lavigne F, Setiawan A, Sartohadi J, Saputra A, Rahardianto T (2021) High-resolution Point-Cloud for Landslides in the 21st Century: From Data Acquisition to New Processing Concepts. In Arbanas Eds. Understanding and Reducing Landslide Disaster Risk, ICL Contribution to Landslide Disaster Risk Reduction, 199-213.
13. Gomez C, Hayakawa Y, Obanawa H (2015) A study of Japanese landscapes using structure from motion derived DSMs and DEMs based on historical aerial photographs: New opportunities for vegetation monitoring and diachronic geomorphology. Geomorphology 242, 11-20.
14. Gomez C, Shinohara Y, Hotta N, Tsunetaka H (2020) In-flow Self-comminution of Debris-flow and Lahars: Fragmentation and Grinding Experiments for the Dacites from Unzen-Volcano. The 10th Symposium of Sediment Hazards, Japanese Society of Civil Engineering Proceedings, 127-132.
15. Gomez C, Soltanzadeh I (2012) Boundary crossing and non-linear theory in earth-system sciences – a proof of concept based on tsunami and post-eruption scenarios on Java Island, Indonesia. Earth Sruface Processes and Landforms 37, 790-796.
16. Gonzalez de Vallejo LI, Jimenez Salas JA, Leguey Jiminez S (1981) Engineering geology of the tropical volcanic soils of La Laguna, Tenerife. Engineering Geology 17, 1-17.
17. Hungr, O. 2005. Classification and terminology. In Jakob and Hungr (Eds.) Debris-flow Hazards and Related Phenomena. Springer, p. 9-24.
18. Iverson, R.M., Schilling, S.P., Vallance, J.W. 1998. Objective delineation of lahar-inundation hazard zones. GSA Bulletin 110-8, 972-984.
19. Kasai M, Yamada T (2019) Topographic effects on frequency-size distribution of landslides triggered by the Hokkaido Eastern Iburi Earthquake in 2018. Earth Planets Space 71:89. https ://doi.org/10.1186/s4062 3-019-1069-8

20. Kobayashi T, Hayashi K, Yarai H (2019b) Geodetically estimated location and geometry of the fault plane involved in the 2018 Hokkaido Eastern Iburi earthquake. Earth Planets Space 71:62. https ://doi.org/10.1186/s40623-019-1042-6
21. Kubo H, Iwaki A, Suzuki W et al (2020) Estimation of the source process and forward simulation of long-period ground motion of the 2018 Hokkaido Eastern Iburi, Japan, earthquake. Earth Planets Space 72:20. https ://doi. org/10.1186/s4062 3-020-1146-z
22. Lagmay AMF, Escape CM, Ybanez AA, Suarez JK, Cuaresma G (2020) Anatomy of the Naga City Landslide and Comparison with Historical Debris Avalanches and Analog Models. Frontiers in Earth Science https://doi.org/10.3389/feart.2020.00312
23. Mateos RM, Azanon JM, Roldan FJ, Notti D, Perez-Pena V, Galve JP, Perez-Garcia JL, Colomo CM, Gomez-Lopez JM, Montserrat O, Devantery N, Lamas-Fernandez F, Fernandez-Chacon F (2017) The combined use of PSInSAR and UAV photogrammetry techniques for the analysis of the kinematics of a coastal landslide affecting an urban area (SE Spain). Landslides 14, 743-754.
24. Morelli S, Prazzi V, Frodella W, Fanti R (2018) Kinematic Reconstruction of a Deep-Seated Gravitational Slope Deformation by Geomophic Analyses. Geosciences 8, 26. https://doi.org/10.3390/geosciences8010026
25. O'Rourke TD, Crespo E (1988) Cemented volcanic soil. ASCE Journal of Geotechnical Engineering 114, 1126-1147.
26. Ohzono M, Takahashi R, Ito C (2019) Spatiotemporal crustal strain distribution around the Ishikari-Teichi-Toen fault zone estimated from global navigation satellite system data. Earth Planets Space 71:50. https ://doi.org/10.1186/s4062 3-019-1024-8
27. Peternal T, Kuemlj S, Ostir K, Komac M (2017) Monitoring the Potoska planina landslide (NW Slovenia) using UAV photogrammetry and tachymetric measurements. Landslides 14, 395-406.
28. Pu X, Wan L, Wang p (2021) Initiation mechanism of mudflow-like loess landslide induced by the combined effect of earthquakes and rainfall. Natural Hazards. https ://doi.org/10.1007/s11069-020-04442-6
29. Rickenmann, D. 2005. Runout prediction methods. In Jakob and Hungr (Eds.) Debris-flow Hazards and Related Phenomena, Springer, p. 305-324.
30. Rickenmann, D. 1999. Empirical relationships for debris flows. Natural Hazards 19, 47-77.
31. Scheidl, C., Rickenmann, D. 2010. Empirical prediction of debris-flow mobility and deposition on fans. Earth Surface Processes and Landforms 35, 157-173.
32. Strozzi T, Ambrosi C (2007) SAR Interferometric Point Target Analysis and Interpretation of Aerial Photographs for Landslides Investigations in Ticino, southern Switzerland. Proceedings of ENVISAT Symposium, Montreux Switzerland.
33. Takahashi, 2014. Debris Flow – Mechanics, Prediction and Countermeasures, 2nd Edition. CRC Press Balkema. P. 540.
34. Takai N, Shigefuji M, Horita J et al (2019) Cause of destructive strong ground motion within 1–2 s in Mukawa town during the 2018 Mw 66 Hokkaido eastern Iburi earthquake. Earth Planets Space 71:67. https ://doi.org/10.1186/s4062 3-019-1044-4
35. Tomas R, Li Z, Lopez-Sanchez JM, Liu P, Singleton A (2016) Using wavelet tools to analyse seasonal variations from InSAR time-series data: A case study of the Huangtupo landslide. Landslides 13, 437-450.
36. Xing A, Wang G, Yin Y, Tang C, Xu Z, Li W (2016) Investigation and dynamic analysis of a catastrophic rock avalanche on September 23, 1991, Zhaotong, China. Landslides 13, 1035-1047.
37. Yamagishi H, Yamazaki F (2018) Landslides by the 2018 Hokkaido Iburi-tobu earthquake on setpember 6. Landslides 15,2521-2524.
38. Yamanouchi T, Murata H (1973) Brittle failure of a volcanic ash soil "Shirasu". In 8th International Conference on Soil Mechanics and Foundation Engineerings, Proceedings Vol. 1, 495-500.

Zhang XJ, Chen WF (1987) Stability analysis of slopes with general nonlinear failure criterion. International Journal of Numerical and Analytical Methods in Geomechanics 11, 33-50.

39. Zhao L-H, Cheng X, Dan H-C, Tang Z-P, Zhang Y (2017) Effect of the vertical earthquake component on permanent seismic displacement of soil slopes based on the nonlinear Mohr-Coulomb failure criterion. Soils and Foundations 57, 237-251.
40. Zhao B, Wang Y, Feng Q, Guo F, Zhao X, Ji F, Liu J, Ming W (2020) Preliminary analysis of some characteristics of coseismic landslides induced by the Hokkaido Iburi-Tobu earthquake (September 5, 2018). Catena 189, 104502. https://doi.org/10.1016/j.catena.2020.104502